

# Helical Intermediate-Period Fiber Grating for Refractive Index Measurements With Low-Sensitive Temperature and Torsion Response

Tao Zou, Junlan Zhong, Shen Liu<sup>1</sup>, Guoxuan Zhu, Yuanyuan Zhao, Junxian Luo, Shengzhen Lu, Qiang Zhang, Jun He<sup>2</sup>, Member, IEEE, Zhiyong Bai<sup>3</sup>, and Yiping Wang<sup>4</sup>, Senior Member, IEEE

**Abstract**—We inscribe and characterize a series of helical intermediate-period fiber gratings (HIPFGs) on single-mode fiber with pitches from 24  $\mu\text{m}$  to 48  $\mu\text{m}$ . The fabricated HIPFGs have low temperature sensitivity, low torsion sensitivity, and high refractive index sensitivity. A series of separated peaks with low insertion losses and high coupling strengths are observed in the transmission spectra of the HIPFGs. For the HIPFG with grating pitch of 36  $\mu\text{m}$  (HIPFG-3), the peaks located at around 1596 nm and 1603 nm are chosen to evaluate the sensor performance of the fiber gratings. The temperature sensitivities are 6.86  $\text{pm}/^\circ\text{C}$  and 7.53  $\text{pm}/^\circ\text{C}$  for peaks around 1596 nm and 1603 nm, respectively. The corresponding values of the torsion sensitivities are 8.67  $\text{nm}/(\text{rad}/\text{mm})$  and 9.49  $\text{nm}/(\text{rad}/\text{mm})$  for those two peaks, respectively. In addition, the average refractive index sensitivity of the grating reaches 393.9  $\text{nm}/\text{RIU}$  in the range of 1.310–1.408. The sensitivity of the HIPFG-3 at the RI of 1.408 is calculated to be 1291  $\text{nm}/\text{RIU}$ . Therefore, we conclude that the HIPFGs proposed in this paper can be used as a high-sensitivity refractive index sensor which is not sensitive to temperature and torsion.

**Index Terms**—Helical intermediate-period fiber gratings, helical grating fabrication system, fiber optics sensors, refractive index sensor.

## I. INTRODUCTION

**L**ONG-PERIOD fiber gratings (LPFGs), which are characterized by insertion loss resistance, ease of fabrication, low

Manuscript received May 11, 2021; revised July 13, 2021; accepted August 4, 2021. Date of publication August 10, 2021; date of current version October 18, 2021. This work was supported in part by The National Natural Science Foundation of China (NSFC) under Grants 61905165, 61875134, and 62005169, in part by the Postdoctoral Science Foundation of China under Grant 2021M692176, in part by the Natural Science Foundation of Guangdong Province under Grants 2018KQNCX219 and 2021A1515011834, and in part by Shenzhen Science and Technology Program under Grants RCBS20200714114922296, JCYJ20180507182058432, and RCYX20200714114538160. (Corresponding author: Shen Liu.)

The authors are with the Shenzhen Key Laboratory of Photonic Devices and Sensing Systems for Internet of Things, College of Physics and Optoelectronic Engineering, Shenzhen University, Shenzhen 518060, China, and also with the Guangdong and Hong Kong Joint Research Centre for Optical Fibre Sensors, Shenzhen University, Shenzhen 518060, China (e-mail: szu\_zoutao@163.com; zhongjunlan1990@gmail.com; shenliu@szu.edu.cn; 1525576362@qq.com; zhaoyi1996@foxmail.com; 479504814@qq.com; rosejenny73@163.com; 1433250143@qq.com; hejun07@szu.edu.cn; baizhiyong@szu.edu.cn; ypwang@szu.edu.cn).

Color versions of one or more figures in this article are available at <https://doi.org/10.1109/JLT.2021.3103550>.

Digital Object Identifier 10.1109/JLT.2021.3103550

back reflection, and high sensitivity, have been widely exploited in a variety of fields, including optical sensors [1], communication [2], neural computing [3], and optical tweezers [4]. Many fabrication methods have been proposed to fabricate fiber gratings on single-mode fibers, such as femtosecond laser direct inscribing [5], CO<sub>2</sub> laser writing [6], direct inscribing [5], CO<sub>2</sub> laser writing [6], laser exposing [7], electric-arc discharging [8], ion-beam irradiation [9], mechanical micro-bending [10]. Refractive index (RI) is an essential parameter used in the LPFGs sensor application. Several methods were proposed to improve the sensitivity for RI sensors. For example, Tsuda *et al.* examined the influence of grating length and bend radius of gratings on refractive index sensing. Their results demonstrated that the RI sensitivity of LPFGs could be modified by changing the grating length and bend radius [11]. Tripathi *et al.* proposed a bio-sensor based on two cascaded dual-resonance long-period fiber gratings with ultra-high sensitivity [12]. Arimand *et al.* reported the internally tilted long-period gratings with refractive index sensitivity up to 100  $\text{nm}/\text{RIU}$  [13]. Recently, by combining thin film materials and fiber sensors, the higher interaction between the evanescent field and the surrounding environment has been enhanced, and higher sensitivity can be obtained [14]–[16]. While, the sensitivity can be improved by changing the cladding diameter [17]–[19]. However when the thickness of the fiber cladding decreases, the grating becomes fragile. But the manufacturing process of these methods is complicated and processing conditions need to be finely controlled. In addition, the inherent high sensitivity of LPFGs, along with other unnecessary interferences, such as temperature and torsion, cause cross-sensitivity in refractive index sensing.

This is an urgent problem to be solved for reliable RI sensing. In this case, Shu *et al.* presented a detailed investigation into the sensitivity of long-period fiber gratings with a period down to 34  $\mu\text{m}$  [20]. The simulation results showed that when the period is as low as tens of micrometers, the sensitivity of temperature and strain is small. Then, the difference between the effective index and the surrounding RI decreased, which causes the sensitivity of RI higher than standard LPFGs. However, LPFGs with a period below 100 micrometers are rarely investigated. Shen *et al.* reported a long-period fiber grating with a period of 25  $\mu\text{m}$  fabricated by UV laser exposing [21]. There are also femtosecond laser processing methods to achieve

the fabrication of small-period long-period gratings [22], [23]. However, these two techniques are not easy to achieve high coupling strengths and low insertion losses. Kopp *et al.* proposed chiral intermediate-period gratings (CIPGs) and studied their polarization characteristics [24]. However, they don't do much research on the sensing characteristics of CIPGs. Here, we first induced hydrogen-oxygen flame heating method for HIPFGs fabrication.

In this paper, we demonstrate a high-efficiency grating fabrication system to write a series of HIPFGs with pitches from 24 to 48  $\mu\text{m}$  in standard single-mode fiber (SMF) by rotating the fiber simultaneously during hydrogen-oxygen flame heating. Comparing with the small-period long-period gratings fabricated by ultraviolet laser exposure [21] or femtosecond laser direct inscribing [22], [23], the fabricated HIPFGs have an ultra-smooth grating surface along the fiber axis direction, a higher coupling strength and a lower insertion loss. Furthermore, we can obtain a large number of HIPFGs with different pitches quickly by simply changing the processing parameters. We also measure the sensing characteristics of the 36  $\mu\text{m}$  pitch sample for the applied temperature, torsion, and refractive index. Experimental results show that the proposed HIPFG has lower temperature sensitivity and torsion sensitivity, and high refractive index sensitivity. The average refractive index sensitivity of the HIPFG-3 reaches 393.9 nm/RIU when the surrounding refractive index changes in the range of 1.310–1.408. The sensitivity of the HIPFG-3 at the RI of 1.408 is calculated to be 1291 nm/RIU.

## II. SENSOR DESIGN AND FABRICATION

In our experiment, the high-efficiency helical grating fabrication system was used to fabricate HIPFGs, which is consisting of a high-precision rotator, two translation stages, and a hydrogen generator. Detailed information about helical grating fabrication system can be found in our previous works [25]. Here, in order to fabricate the HIPFGs, we have replaced the motor with high rotated rate, modified the processing conditions, in the helical grating fabrication system. The HIPFG's pitch is calculated by:

$$\Lambda = 60V_2/\Omega \quad (1)$$

where,  $\Omega$  (rpm) is a rotated rate,  $V_2$  (mm/s) is a moving velocity of translation stage, respectively. Therefore, the HIPFGs can be obtained by increasing the rotated rate of motor or reducing the moving velocity of the translation stage. For example, in our experiment, we replace a motor with a faster rotated rate, which is set to 3000 rpm with reducing the velocity of the translation stage to 1.2 mm/s, and then, a HIPFG sample could be fabricated with a grating pitch of 24  $\mu\text{m}$ . We designed and fabricated five samples (HIPFG-1, HIPFG-2, HIPFG-3, HIPFG-4, and HIPFG-5), and the corresponding grating pitches are 24  $\mu\text{m}$ , 30  $\mu\text{m}$ , 36  $\mu\text{m}$ , 42  $\mu\text{m}$ , and 48  $\mu\text{m}$ , respectively. The HIPFGs lengths of five samples are cut to be about 20.0 mm, 22.0 mm, 17.5 mm, 15.5 mm, and 16.0 mm, respectively. The transmission spectra of the sampled gratings are monitored by using an amplified spontaneous emission source (ASE, NKT Photonics) and an optical spectrum analyzer (OSA, YOKOGAWA, AQ6370C) with a resolution of 0.02 nm. The transmission spectra of the

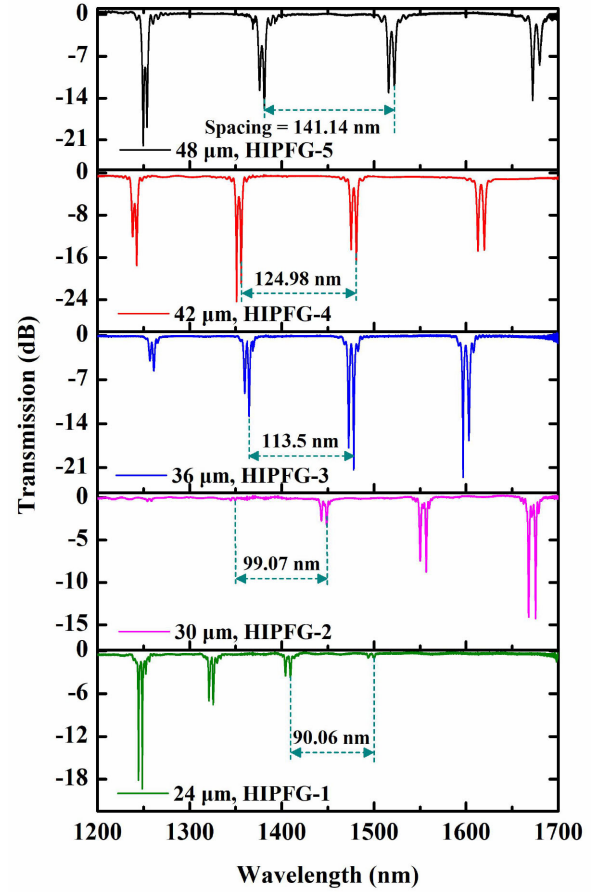


Fig. 1. The transmission spectra of five fabricated HIPFG samples (HIPFG-1, HIPFG-2, HIPFG-3, HIPFG-4, and HIPFG-5).

fabricated HIPFGs are shown in Fig. 1. The helical LPFG's resonant wavelength and coupling strength of resonance peak are strictly depended on the grating pitches and numbers of grating pitches (i.e., grating length), respectively, this conclusion is discussed in detail in reference [26]. A series of separated peaks appear in the transmission spectra of samples with different grating pitches. When the pitch increases from 24  $\mu\text{m}$  to 48  $\mu\text{m}$  with a step of 6  $\mu\text{m}$ , the spacing between adjacent two sets of separated peaks are 90.06 nm, 99.07 nm, 113.5 nm, 124.98 nm, and 141.14 nm, respectively. Therefore, as the grating pitch decreases, the spacing between the adjacent two sets of separated peaks becomes smaller. All samples have high-quality transmission spectra and the coupling strengths, of which a maximum more than -20 dB. And the full width at half-maximum (FWHM) of the HIPFG is only about 3 nm, which is narrower than that of reported value 20 to 30 nm of the normal LPFG with a pitch around 550 to 600  $\mu\text{m}$  [27]). For complete transfer, the  $\Delta\lambda$  (FWHM) of LPFG can be given approximately by:

$$\Delta\lambda \approx \frac{0.8\lambda^2}{L \left( n_{eff}^{co} - n_{eff}^{cl,m} \right)} \quad (2)$$

where,  $L$  is the grating length,  $n_{eff}^{co}$  and  $n_{eff}^{cl,m}$  are the effective indexes of the fundamental core mode and the  $m$ th cladding

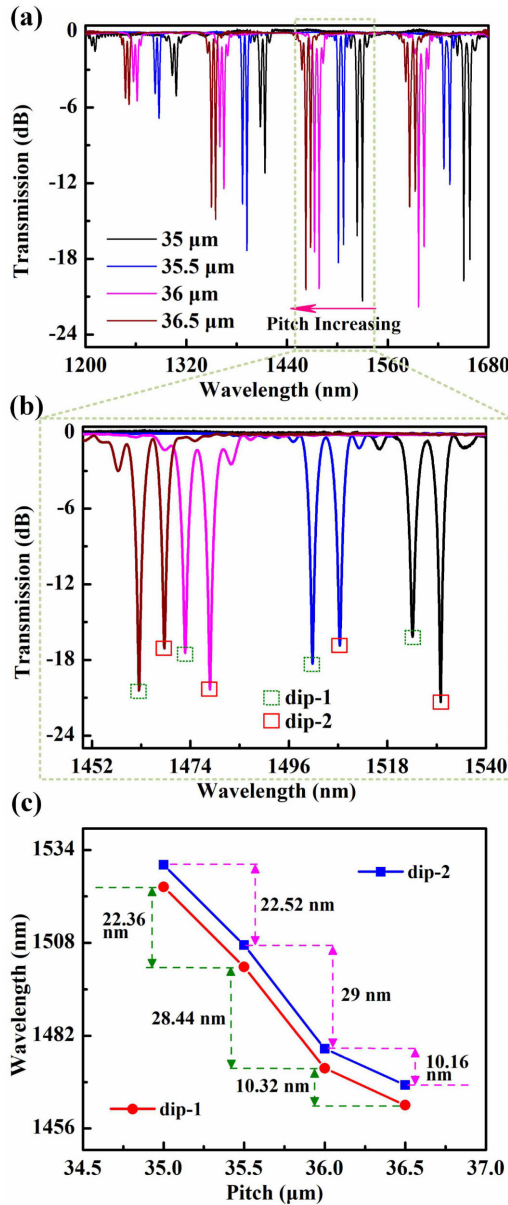


Fig. 2. (a) The spectral evolution of four HIPFG samples. (b) The zoomed-in transmission spectrum covering the wavelength range from 1450 to 1540 nm. (c) Variations of the resonance wavelength of four samples with different pitches.

mode, respectively. Moreover, the order of the cladding mode increases with the grating pitch decreasing, resulting in the smaller value of the  $n_{eff}^{cl,m}$  [28]. So, the pitch of our HIPFG is much smaller than that of a normal LPFG, according to equation (2), it can be calculated that the  $\Delta\lambda$  (FWHM) of the HIPFG is narrower than that of a normal LPFG. These features provide a favorable condition for sensor application.

In order to obtain the spectral evolution of the HIPFGs with different pitches, four samples were designed and fabricated with a pitch step of 0.5 μm. The grating pitches are 35 μm, 35.5 μm, 36 μm, and 36.5 μm, respectively. The transmission spectra are shown in fig. 2(a), it can be seen that the resonance peak shifts to the short-wavelength direction with the grating

pitch increasing. The coupling strengths of the four samples can reach more than -20 dB and insertion losses are measured to less than 0.1 dB.

Fig. 2(b) shows the zoomed-in transmission spectrum covering the wavelength range from 1450 to 1540 nm. Within this wavelength range, the peaks in the green dashed box in the spectrum are named dip-1, and the peaks in the red solid box are named dip-2. Fig. 2(c) shows variations of the resonance wavelength of four samples with different pitches. When the pitch increases from 35 μm to 36.5 μm with a step of 0.5 μm, the dip-1 shift toward a shorter wavelength direction, and the corresponding variations are 22.52 nm, 29.0 nm, and 10.16 nm, respectively. And the dip-2 also shift toward a shorter wavelength direction, the corresponding variations are 22.36 nm, 28.44 nm, and 10.32 nm, respectively. In short, when the grating period increases by 0.5 μm, the dip-1 and the dip-2 shift toward a shorter wavelength direction with 20.6 nm and 20.4 nm on average, respectively. The processing accuracy of the system has reached the sub-micron scale.

### III. ANALYSIS OF GRATING

In the following content, the HIPFG-3 sample is chosen as a research example, to study the structure and the polarization characteristics of our grating samples.

The transmission spectrum of the fabricated HIPFG-3 is shown in Fig. 3(a). Four sets of separated peaks are observed around 1259 nm, 1362 nm, 1475 nm, and 1600 nm in the transmission spectrum. The peak separation gap of HIPFG-3 is increasing as wavelength increasing which are 4.33 nm, 4.83 nm, 5.46 nm, and 6.45 nm in sequence. As shown in the figure, the coupling strength at longer wavelengths is deeper than the coupling strength at shorter wavelengths. Fig. 3(b), enlarging view of the separated peaks, shows the transmission spectrum of HIPFG-3 with a wavelength range from 1590 to 1610 nm. The coupling strengths of dip-1 and dip-2 can reach -22.94 dB and -17.02 dB at 1596.8 nm and 1603.3 nm, respectively. And the insertion loss of the grating is as low as 0.1 dB. To investigate the actual structure of the HIPFG-3 sample, we obtained an optical microscope image and a scanning electron microscope (SEM) image of the sample. Fig. 3(c) shows the structure of the fabricated HIPFG-3 sample observed by the optical microscope along the fiber-axis direction of optical fiber. We can see the periodic RI perturbations in the SMF. The actual structure of the fiber axial surface is obtained by SEM, as shown in Fig. 3(d). There is no mechanical deformation on the surface of the HIPFG-3 sample.

As shown in Fig. 3(a), a strong peak splitting is observed. The reason is that the intrinsic properties of high-order cladding modes in single-mode fiber, which are far away from weakly guided regime. Thus, we should take their vectorial nature and degeneracies into account [22], [29], [30]. To further analyze the reason for the peak splitting, the near field mode beam profiles of the separated peaks in the HIPFG-3 sample are detected. The light from a tunable laser is propagated into the grating sample which is cleaved at the last grating period and fixed by the fiber clamp, and then the beam is collimated into an infrared camera

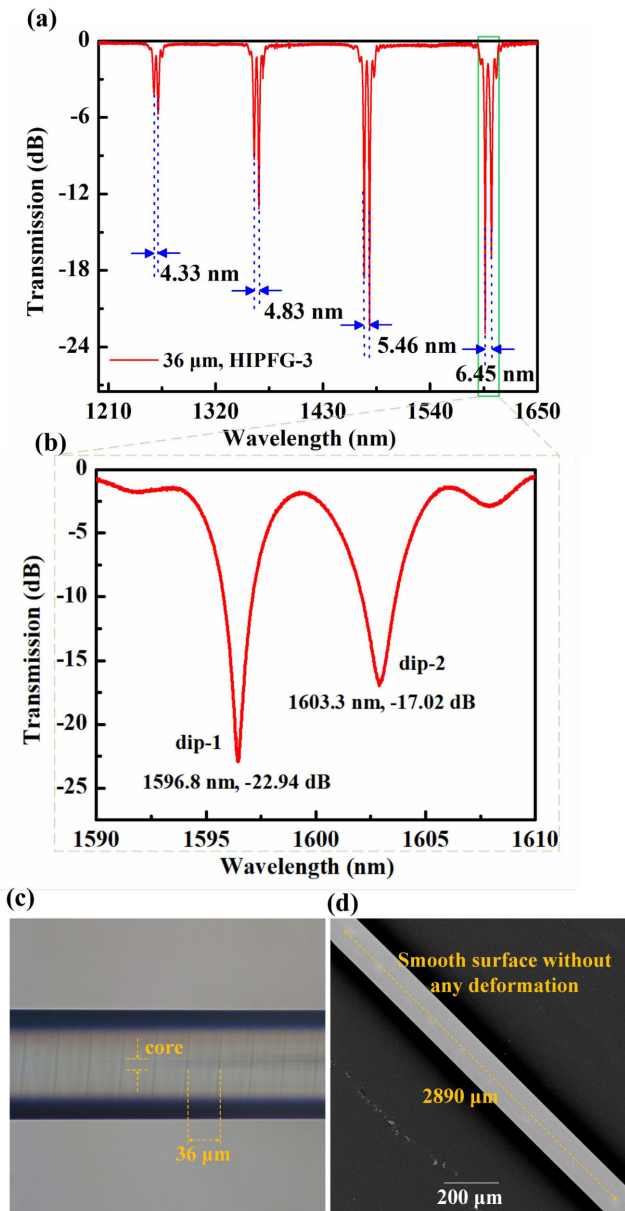


Fig. 3. (a) The transmission spectrum of HIPFG-3. (b) The transmission spectrum of HIPFG-3 with a wavelength range of 1590 nm-1610 nm. (c) Microscope imaging of the fabricated HIPFG-3. (d) The SEM along the fiber axis direction of the fabricated HIPFG-3.

through a lens. The dip-1 and dip-2 at resonant wavelengths of around 1597 and 1604 nm shown in Fig. 3(b) have the same orders of 26<sup>th</sup> cladding modes, as shown in Figs. 4 (a) and (b). Similarly, the same orders of 27<sup>th</sup> cladding modes at the resonant wavelengths of 1475 and 1581 nm for another set of separated peaks were also observed, as shown in Figs. 4 (c) and (d). Therefore the peak splitting is a result of fundamental core mode coupling to two polarization states of the same high-order cladding modes.

Next, we select the two wavelengths range of 1596 -1597.5 nm and 1601.5 -1605 nm in the original spectrum for the polarization-dependent loss (PDL) measurement to study the polarization characteristics. The PDL of sample HIPFG-3 is

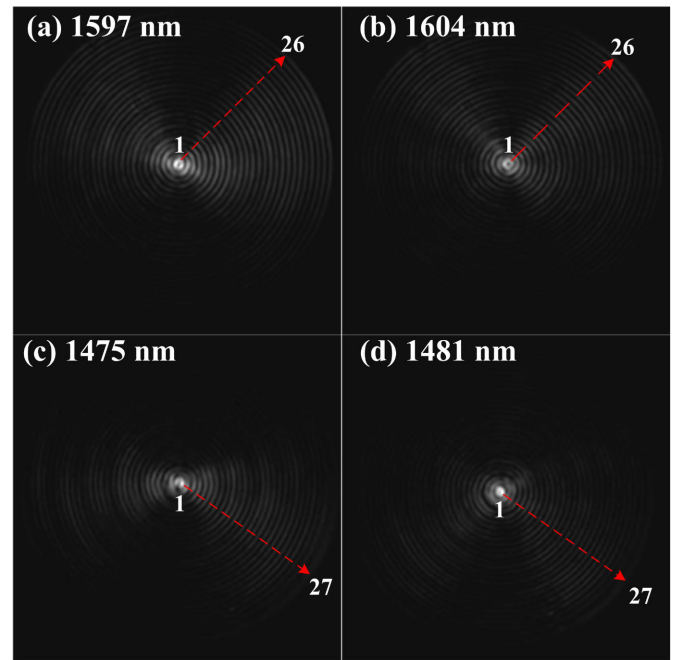


Fig. 4. (a), (b), (c), (d) Beam profiles generated by the inscribed HIPFG-3 at the wavelength of 1597, 1604, 1475, and 1481 nm, respectively.

measured at the splitting of resonance peaks and the instruments for measuring PDL include a tunable laser source (Keysight Model N7776C), a polarization synthesizer (Keysight Model N7788C), and an optical power meter (Agilent Model N7744A). Fig. 5(a) shows the TE, TM, and PDL spectra of the HIPFG-3 at around dip-1. The PDL of the grating sample at a wavelength of 1596.9 nm is -16.54 dB and the wavelength spacing between dip-1 and dip-2 is about 0.27 nm. The TE, TM, and PDL spectra of the HIPFG-3 at around dip-2 is shown in fig. 5(b). The PDL of the HIPFG-3 at 1603.1 nm is -11.35 dB and the wavelength spacing between dip-1 and dip-2 is about 0.47 nm. The strong polarization dependence is mainly due to the asymmetric azimuth profile of the refractive index modulation in the helical fiber.

#### IV. REFRACTIVE INDEX MEASUREMENT AND DISCUSSION

We measured and characterized the sensing characteristics of refractive index of the 36  $\mu\text{m}$  pitch sample. The refractive index matching liquid provided by Cargille Labs was applied for the RI measurement. When testing the refractive index sensing characteristics, the entire HIPFG-3 sample was immersed in the refractive index matching liquid and the spectra were recorded after the spectra stabilized. After each measurement, the surface of the tested sample was wiped off by ethanol to restore the spectrum back to the original spectrum state. Fig. 6(a) shows the HIPFG-3 transmission spectra in air and different surrounding liquids with a refractive index range from 1.310 to 1.408. We can see that as the refractive index increases, the peak shifts toward the long-wavelength direction. When the refractive index is above 1.375, the double resonance peaks shift into a single peak, owing to the effective refractive indexes of these two vector modes are different [28], [31]. Furthermore, the mode indexes

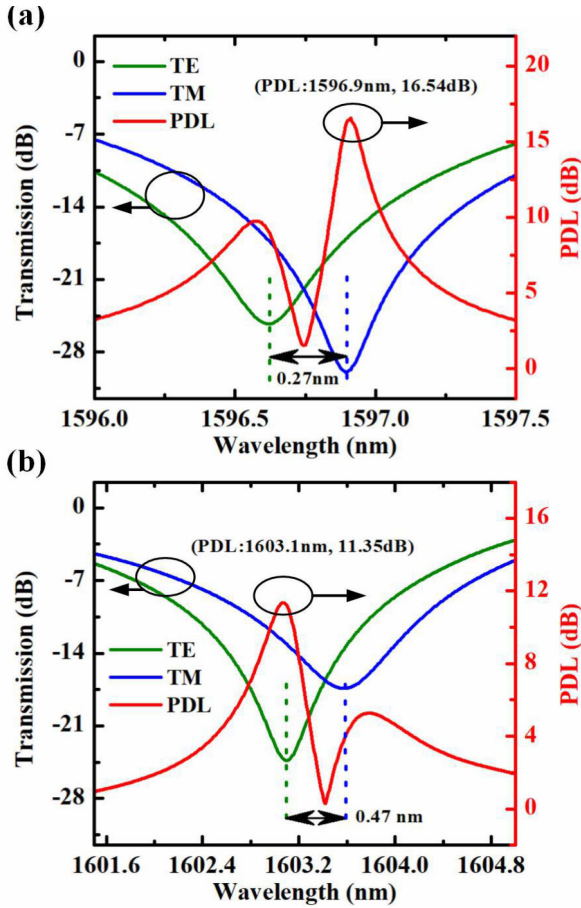


Fig. 5. (a) The transmission spectrum of the HIPFG-3 with a wavelength range from 1590 to 1610 nm. (b) Measurement results for the TE, TM, and PDL spectra of the HIPFG-3.

of these two polarization states vector modes vary and the index difference between these two modes decreases as the refractive index increases. Therefore, the separated peaks of HIPFGs overlap together for RI above 1.375, and only one resonance peak is observed in the transmission spectrum, as shown in Fig. 6(a). Fig. 6(b) depicts the shift of the long-wavelength side resonance peak as the refractive index changes. The sensor's refractive index sensitivity appears to a nonlinear increase with the surrounding refractive index increasing. When the surrounding refractive index increases from 1.310 to 1.408, the wavelength change is 38.6 nm and the average refractive index sensitivity is 393.9 nm/RIU. As the value of the refractive index increases, the sensor sensitivity increases. The sensitivity of the HIPFG-3 at the RI of 1.408 is calculated to be 1291 nm/RIU.

## V. TEMPERATURE MEASUREMENT

We also evaluated the temperature independence of the sample HIPFG-3. In the measurement, a column oven (LCO 102, ECOM) with an accuracy of 0.1°C was utilized and the temperature range was set from 20°C to 100°C in steps of 10°C. The spectrum is shown in Fig. 7(a). As shown in the figure, as the temperature increases, the resonance wavelength shifts to a longer wavelength. The linear fitting diagram of the measured

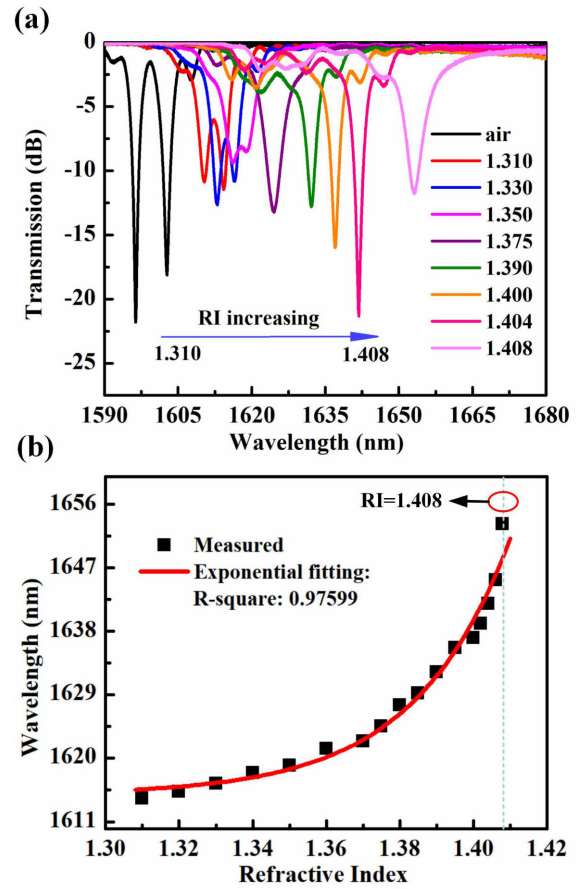


Fig. 6. (a) HIPFG-3 transmission spectra in air and different surround refractive index. (b) Relationship between resonant dip wavelength and the surrounding RI.

temperature is shown in Fig. 7(b). The temperature sensitivities for the dips around 1596 and 1603 nm are 6.86 pm/°C and 7.53 pm/°C, respectively. This is far lower than the normal helical long-period fiber gratings with a pitch around 600 to 900  $\mu\text{m}$  reported in [18] with a temperature sensitivity of  $\sim 80$  pm/°C. The sensing characteristics of long-period fiber gratings are described in detail in the Ref. [20]. The temperature sensitivity of the long-period fiber gratings can be calculated by,

$$\frac{d\lambda_{res}}{dT} = \lambda_{res} \cdot \gamma \cdot (\alpha + \Gamma_{temp}) \quad (3)$$

where,  $\lambda_{res}$  is the resonance wavelength,  $\gamma$  is the waveguide dispersion factor,  $\alpha$  is the thermal expansion coefficient of the fiber, and  $\Gamma_{temp}$  is the sensitivity factor of temperature. Compared with the standard long-period fiber gratings, the HIPFGs have higher-order cladding modes and smaller effective refractive indexes, which result in a smaller waveguide dispersion factor  $\gamma$  and temperature sensitivity factor  $\Gamma_{temp}$ , so the temperature sensitivity of HIPFGs is lower than that of the LPFGs calculated by Eq.(3). This result demonstrates that the HIPFG-3 can greatly reduce influence caused by temperature.

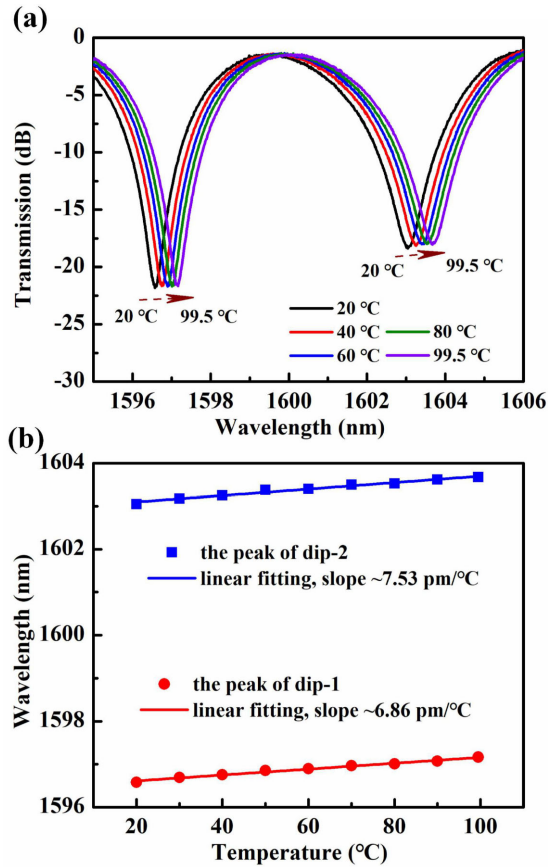


Fig. 7. (a) The spectral evolution of the HIPFG-3 with the temperature rising from 20°C to 99.5°C. (b) The corresponding temperature response of the HIPFG-3.

## VI. TORSION MEASUREMENT

To evaluate the torsion sensing characteristics of HIPFGs, we measured the torsional response of the sample HIPFG-3. During the measurement, one end of the sample was fixed on a rotating table, which provided a precise rotation angle, and another end of the sample was fixed on a fixed stage. The clockwise direction corresponds to the helical direction of the measured HIPFG-3 sample, and the counter-clockwise direction is opposite to the helical direction of the HIPFG-3. The spectra are recorded at each twist angle and the result is shown in Fig. 8(a). The dotted line corresponds to the resonant peak position of the original spectrum when the torsion angle is 0°. The torsion angle increases from 0° to +360° (clockwise) and -360° (counter-clockwise) with the step of 120°. When the grating is twisted clockwise, the resonance wavelength shifts toward a long-wavelength direction. On the contrary, the resonance wavelength shifts toward a short-wavelength direction. Then the torsional sensitivity is calculated by linear fitting the experimental data at room temperature shown in Fig. 8(b), the values of the torsion sensitivity of the dip-1 and dip-2 are measured to be about 8.67 and 9.49 nm/(rad/mm), which are much smaller than that of reported values in Ref. [32~35] of 103, 76, 46.46 and 96.4 nm/(rad/mm), corresponding to different pitches of 500, 630, 450 and 550  $\mu\text{m}$ , respectively. The principle

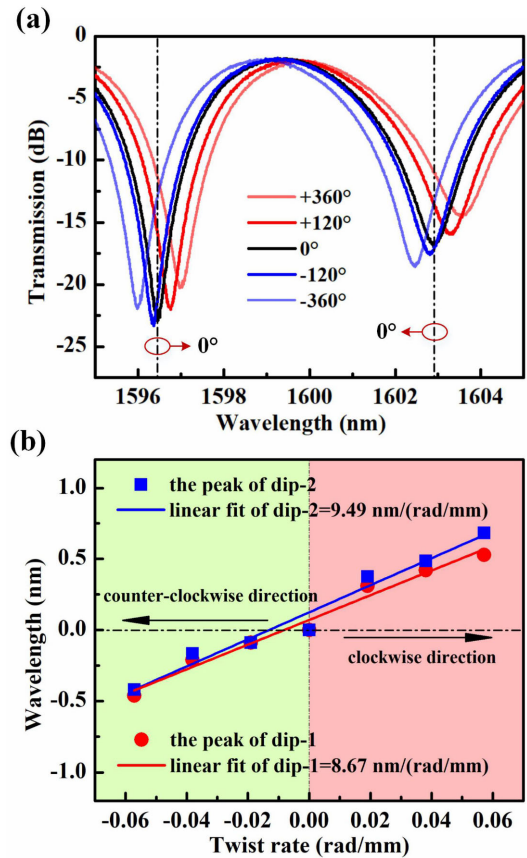


Fig. 8. (a) The spectral evolution of the HIPFG-3 with varying torsion angles. (b) The corresponding wavelength shift for an applied torsion angle.

for the torsion sensing is similar to that of the strain sensing, which in fact is the HIPFGs response to the stress. When the twisted stress is applied to HIPFGs, the grating period decreases or increases, depending on the twisted direction, i.e., clockwise or anticlockwise. Here, the strain sensitivity of the long-period fiber gratings can be calculated by [20]:

$$\frac{d\lambda_{res}}{d\varepsilon} = \lambda_{res} \cdot \gamma \cdot (1 + \Gamma_{strain}) \quad (4)$$

where,  $\Gamma_{strain}$  is the sensitivity factor of strain. Similarly, compared with the long-period fiber gratings, HIPFGs have a smaller strain sensitivity factor  $\Gamma_{strain}$ , so the strain sensitivity of HIPFGs is lower than that of the LPFGs calculated by Eq.(4). Therefore, we conclude that the influence caused by torsion is relatively low.

## VII. CONCLUSION

In this study, we propose and demonstrate a series of helical intermediate-period fiber gratings fabricated on single-mode fiber with pitches from 24  $\mu\text{m}$  to 48  $\mu\text{m}$ . The HIPFGs are fabricated by rotating the fiber simultaneously during hydrogen-oxygen flame heating. This fabrication method is low cost, high efficiency, and easy production of different grating pitches. The HIPFGs have high coupling strengths and low insertion losses, the average refractive index sensitivity of the grating with a pitch

of 36  $\mu\text{m}$  reaches 393.9 nm/RIU in the range of 1.310–1.408. The sensitivity of the tested HIPFG at the RI of 1.408 is calculated to be 1291 nm/RIU. And the tested HIPFG exhibits low-temperature sensitivities of 6.86 pm/ $^{\circ}\text{C}$  and 7.53 pm/ $^{\circ}\text{C}$  at peaks around 1596 nm and 1603 nm, respectively. And the torsion sensitivities of the two peaks are 8.67 nm/(rad/mm) and 9.49 nm/(rad/mm), respectively. Therefore, the cross-sensitivity caused by temperature and torsion is greatly reduced. In conclusion, the HIPFGs proposed in this paper can be used as a high-sensitivity refractive index sensor that is not sensitive to temperature and torsion.

## REFERENCES

- [1] Y. P. Wang, "Review of long period fiber gratings written by laser," *J. Appl. Phys.*, vol. 108, no. 8, Aug. 2010, Art. no. 081101.
- [2] Y. J. Rao, T. Zhu, Z. L. Ran, Y. P. Wang, J. Jiang, and A. Z. Hu, "Novel long-period fibre gratings written by high-frequency CO<sub>2</sub> laser pulses and applications in optical fibre communication," *Opti. Commun.*, vol. 229, no. 1, pp. 209–221, Jan. 2004.
- [3] J. Sun, C. Chan, K. Tan, X. Dong, and P. Shum, "Application of an artificial neural network for simultaneous measurement of bending curvature and temperature with long period fiber gratings," *Sens. Actuat. A Phys.*, vol. 137, no. 2, pp. 262–267, Jul. 2007.
- [4] M. J. Padgett and R. Bowman, "Tweezers with a twist," *Nature Photon.*, vol. 5, no. 6, pp. 343–348, Jun. 2011.
- [5] A. Wolf, A. Dostovalov, I. Lobach, and S. Babin, "Femtosecond laser inscription of long-period fiber gratings in a polarization maintaining fiber," *J. Lightw. Technol.*, vol. 33, no. 24, pp. 5178–5183, Dec. 2015.
- [6] Y. Rao, Y. Wang, Z. Ran, and T. Zhu, "Novel fiber-optic sensors based on long-period fiber gratings written by high-frequency CO<sub>2</sub> laser pulses," *J. Lightw. Technol.*, vol. 21, no. 5, pp. 1320–1325, May 2003.
- [7] L. Jin, Z. Wang, Y. Liu, G. Kai, and X. Dong, "Ultraviolet-inscribed long period gratings in all-solid photonic bandgap fibers," *Opt. Exp.*, vol. 16, no. 25, pp. 21119–21131, Dec. 2008.
- [8] G. Yin, J. Tang, C. Liao, and Y. Wang, "Automatic arc discharge technology for inscribing long period fiber gratings," *Appl. Opt.*, vol. 55, no. 14, pp. 3873–3878, May 2016.
- [9] M. L. von Bibra, A. Roberts, and J. Canning, "Fabrication of long-period fiber gratings by use of focused ion-beam irradiation," *Opt. Lett.*, vol. 26, no. 11, pp. 765–767, Jun. 2001.
- [10] I. K. Hwang, S. H. Yun, and B. Y. Kim, "Long-period fiber gratings based on periodic microbends," *Opt. Lett.*, vol. 24, no. 18, pp. 1263–1265, Sep. 1999.
- [11] H. Tsuda and K. Urabe, "Characterization of long-period grating refractive index sensors and their applications," *Sensors*, vol. 9, no. 6, pp. 4559–4571, 2009.
- [12] S. M. Tripathi, W. J. Bock, and P. Mikulic, "A wide-range temperature immune refractive-index sensor using concatenated long-period-fiber-gratings," *Sens. Actuat. B-Chem.*, vol. 243, pp. 1109–1114, 2017.
- [13] M. Arjmand, F. Chiavaioli, S. Berneschi, F. Baldini, M. Soltanolkotabi, and C. Trono, "Effect of induced inner curvature on refractive index sensitivity in internally tilted long-period gratings," *Opt. Lett.*, vol. 41, no. 7, pp. 1443–1446, Apr. 2016.
- [14] L. Melo, G. Burton, P. Kubik, and P. Wild, "Long period gratings coated with hafnium oxide by plasma-enhanced atomic layer deposition for refractive index measurements," *Opt. Exp.*, vol. 24, no. 7, pp. 7654–7669, Apr. 2016.
- [15] Z. Li and H. Zhu, "Sensing performance of surface waveguide modes excited in long-period fiber grating with gold-silicon nanocoatings," *Opt. Lett.*, vol. 46, no. 2, pp. 266–269, Jan. 2021.
- [16] J. Dong *et al.*, "Refractive index sensor based on graphene oxide-coated long-period fiber grating inscribed in a two-mode fiber," *IEEE Access*, vol. 8, pp. 109028–109037, 2020.
- [17] P. Fan, L. P. Sun, Z. Yu, J. Li, C. Wu, and B. O. Guan, "Higher-order diffraction of long-period microfiber gratings realized by arc discharge method," *Opt. Exp.*, vol. 24, no. 22, pp. 25380–25388, Oct. 2016.
- [18] Y. Zhao *et al.*, "Torsion, refractive index, and temperature sensors based on an improved helical long period fiber grating," *J. Lightw. Technol.*, vol. 38, no. 8, pp. 2504–2510, Apr. 2020.
- [19] S. Prashar, S. Singh, D. Engles, and S. Kaushik, "2-layer and 3-layer fiber geometry model based analysis of refractive index sensitivity of long period fiber grating with reduced cladding," *J. Optoelectron. Adv. M.*, vol. 21, no. 5-6, pp. 295–301, Jun. 2019.
- [20] X. Shu, L. Zhang, and I. Bennion, "Sensitivity characteristics of long period fiber gratings," *J. Lightw. Technol.*, vol. 20, no. 2, pp. 255–266, Feb. 2002.
- [21] F. Shen, C. Wang, Z. Sun, K. Zhou, L. Zhang, and X. Shu, "Small-period long-period fiber grating with improved refractive index sensitivity and dual-parameter sensing ability," *Opt. Lett.*, vol. 42, no. 2, pp. 199–202, Jan. 2017.
- [22] F. Shen, K. Zhou, N. Gordon, L. Zhang, and X. Shu, "Compact eccentric long period grating with improved sensitivity in low refractive index region," *Opt. Exp.*, vol. 25, no. 14, pp. 15729–15736, Jul. 2017.
- [23] Z. Zheng, Y. Yu, X. Zhang, Q. Guo, and H. Sun, "Femtosecond laser inscribed small-period long-period fiber gratings with dual-parameter sensing," *IEEE Sens. J.*, vol. 18, no. 3, pp. 1100–1103, Feb. 2018.
- [24] V. I. Kopp, V. M. Churikov, J. Singer, N. Chao, D. Neugroschl, and A. Z. Genack, "Chiral fiber gratings," *Science*, vol. 305, no. 5680, pp. 74–75, Jul. 2004.
- [25] Z. Li *et al.*, "Residual-stress-induced helical long period fiber gratings for sensing applications," *Opt. Exp.*, vol. 26, no. 18, pp. 24114–24123, Sep. 2018.
- [26] C. Fu *et al.*, "Orbital angular momentum mode converter based on helical long period fiber grating inscribed by hydrogen-oxygen flame," *J. Lightw. Technol.*, vol. 36, no. 9, pp. 1683–1688, 2018.
- [27] A. M. Vengsarkar, P. J. Lemaire, J. B. Judkins, V. Bhatia, T. Erdogan, and J. E. Sipe, "Long-period fiber gratings as band-rejection filters," *J. Lightw. Technol.*, vol. 14, no. 1, pp. 58–65, 1996.
- [28] Z. Yan *et al.*, "Theoretical and experimental analysis of excessively tilted fiber gratings," *Opt. Exp.*, vol. 24, no. 11, pp. 12107–12115, 2016.
- [29] J. U. Thomas *et al.*, "Cladding mode coupling in highly localized fiber Bragg gratings. II: Complete vectorial analysis," *Opt. Exp.*, vol. 20, no. 19, pp. 21434–21449, 2012.
- [30] M. Z. Alam and J. Albert, "Selective excitation of radially and azimuthally polarized optical fiber cladding modes," *J. Lightw. Technol.*, vol. 31, no. 19, pp. 3167–3175, 2013.
- [31] T. Lu, "Excessively tilted fiber grating-based vector magnetometer," *Opt. Lett.*, vol. 44, no. 10, pp. 2494–2497, 2019.
- [32] Z. Han *et al.*, "A polarization-independent torsion sensor based on the near-helical long period fiber grating," *Chin. Opt. Lett.*, vol. 16, no. 10, Oct. 2018, Art. no. 100601.
- [33] L. Xian, D. Wang, and L. Li, "Torsion and strain simultaneous measurement using a cascaded helical long-period grating," *J. Opt. Soc. Amer. B*, vol. 37, no. 5, pp. 1307–1311, May 2020.
- [34] B. Sun *et al.*, "Automatic arc discharge-induced helical long period fiber gratings and its sensing applications," *IEEE Photon. Technol. Lett.*, vol. 29, no. 11, pp. 837–876, Jun. 2017.
- [35] X. P. Wang, D. D. Wang, Q. Wang, L. L. Xian, and L. Li, "Fabrication and characterization of helical long-period fiber gratings in single-mode fibers," *Optik*, vol. 158, pp. 28–32, Dec. 2018.

**Tao Zou** was born in Hunan, China, in 1997. He received the B.E. degree in opto-electronics information science and engineering from the Guilin University of Electronic Technology, Guilin, China, in 2019. His current research focuses on the design and fabrication of helical fiber grating devices and their applications.

**Junlan Zhong** was born in Jiangxi, China, in 1990. She received the B.E. degree in engineering in biomedical engineering from Jinggangshan, China, in 2013, the M.S. degree in engineering in biomedical engineering from Shenzhen University, Shenzhen, China, in 2016, and the Ph.D. degree in philosophy in environment studies from the University of Tsukuba, Tsukuba, Japan, in 2017. Since October 2020, she has been with Shenzhen University as a Postdoctoral. Her current research interests include optical fiber sensors, WGMs resonators, and biosensors.

**Shen Liu** was born in Henan, China, in 1986. He received the B.E. degree in electronic and information engineering from PLA Air Force No.1 Aviation University, Changchun, China, in 2008, the M.S. degree in circuit and system from the Chongqing University of Posts and Telecommunications, Chongqing,

China, in 2013, and the Ph.D. degree in optics from Shenzhen University, Shenzhen, China, in 2017. From 2017 to 2018, he was with Aston University, Birmingham, U.K., as a Postdoctoral Fellow. Since September, 2018, he has been with Shenzhen University as an Assistant Professor. He has authored or coauthored 11 patent applications and more than 90 journal and conference papers. His current research interests include optical fiber sensors, WGMS resonator, and cavity optomechanics.

**Guoxuan Zhu** was born in Nanjing city, China, in 1992. He received the B.S. and Ph.D. degrees in optical engineering from Sun Yat-sen University, Guangzhou, China, in 2014 and 2019, respectively. From 2018 to 2019, he was with the Optoelectronics Research Centre, University of Southampton, Southampton, U.K., as a Scholar Visitor. Since 2019, he has been a Postdoctoral Researcher with the Guangdong and Hong Kong Joint Research Centre for Optical Fiber Sensors, Shenzhen University, Shenzhen, China. His current research interests include optical fiber, fiber communication, space-division multiplexing, fiber gratings, and optical orbital angular momentum.

**Yuanyuan Zhao** was born in Jilin, China, in 1996. She received the B.S. degree in electronic science and technology from the Changchun University of Science and Technology, Changchun, China, in 2018. Her current research interests include design and fabrication of novel fiber grating devices and their applications in sensor devices.

**Junxian Luo** was born in Guangxi, China, in 1996. She received the B.E. degree in opto-electronics information science and engineering from the Guilin University of Electronic Technology, Guilin, China, in 2018. Her current research interests include optical fiber resonator and phase-shifted Bragg grating based on femtosecond laser micro-processing technology.

**Shengzhen Lu** was born in 1997. She received the B.S. degree in physics from Lingnan Normal University, Zhanjiang, China, in 2019. She is currently working toward the master's degree in optical engineering with Shenzhen University, Shenzhen, China. Her major research focuses on high-Q WGMS resonator.

**Qiang Zhang** was born in Hebei, China, in 1997. He received the B.S. degree in opto-electronics information science and engineering from Xiangtan University, Xiangtan, China, in 2019. His current research focuses on optical fiber resonator.

**Jun He** (Member, IEEE) was born in Hubei, China, in 1985. He received the B.Eng. degree in electronic science and technology from Wuhan University, Wuhan, China, in 2006 and the Ph.D. degree in electrical engineering from the Institute of Semiconductors, Chinese Academy of Sciences, Beijing, China, in 2011. From 2011 to 2013, he was with Huawei Technologies, Shenzhen, China, as a Research Engineer. From 2013 to 2015, he was affiliated with Shenzhen University, Shenzhen, China, as a Postdoctoral Research Fellow. From 2015 to 2016, he was with The University of New South Wales, Sydney, NSW, Australia, as a Visiting Fellow. Since 2017, he has been with Shenzhen University, Shenzhen, China, as an Assistant Professor. His current research interests include optical fiber sensors, fiber Bragg gratings, and fiber lasers. He has authored or coauthored four patent applications and more than 80 journal and conference papers. He is a Member of the Optical Society of America.

**Zhiyong Bai** received the B.S. degree in physics from Ningbo University, Ningbo, China, in 2008, the M.S. degree in optics from South China Normal University, Guangzhou, China, in 2011, and the Ph.D. degree in optics from Nankai University, Tianjin, China in 2014. From 2014 to 2015, he has with the State Grid Electric Power Research Institute, as a R&D Engineer. Since 2015, he has been a Postdoctoral Research Fellow with the Guangdong and Hong Kong Joint Research Centre for Optical Fiber Sensors, Shenzhen University, Shenzhen, China. He is the author or coauthor of more than 30 journal papers. His current research interests include optical fiber gratings, orbital angular momentum, and optical fiber sensors.

**Yiping Wang** (Senior Member, IEEE) was born in Chongqing, China, in 1971. He received the B.Eng. degree in precision instrument engineering from the Xi'an Institute of Technology, Xi'an, China, in 1995 and the M.S. degree and Ph.D. degree in optical engineering from Chongqing University, Chongqing, China, in 2000 and 2003, respectively. From 2003 to 2005, he was with Shanghai Jiao Tong University, Shanghai, China, as a Postdoctoral Fellow. From 2005 to 2007, he was with the Hong Kong Polytechnic University, Hong Kong, as a Postdoctoral Fellow. From 2007 to 2009, he was with the Institute of Photonic Technology, Jena, Germany, as a Humboldt Research Fellow. From 2009 to 2011, he was with the Optoelectronics Research Centre, University of Southampton, Southampton, U.K., as a Marie Curie Fellow. Since 2012, he has been with Shenzhen University, Shenzhen, China, as a Distinguished Professor. He has authored or coauthored one book, 21 patent applications, and more than 240 journal and conference papers. His current research interests include optical fiber sensors, fiber gratings, and photonic crystal fibers. His current research interests include optical fiber sensors, fiber gratings, and photonic crystal fibers. He is a Senior Member of the Optical Society of America and the Chinese Optical Society.